

# Strain-tuning of domain walls in multilayer graphene probed in the quantum Hall regime

Paul Anderson,<sup>1</sup> Yifan Huang,<sup>2</sup> Yuanjun Fan,<sup>2</sup> Sara Qubbaj,<sup>1</sup>

Sinisa Coh,<sup>3</sup> Qin Zhou,<sup>2</sup> and Claudia Ojeda-Aristizabal<sup>1</sup>

<sup>1</sup>*Department of Physics and Astronomy,  
California State University Long Beach,  
Long Beach, California 90840, USA\**

<sup>2</sup>*Department of Mechanical and Materials Engineering,  
University of Nebraska, Lincoln 68588-0526, Nebraska, USA\**

<sup>3</sup>*Department of Mechanical Engineering and Materials Science and Engineering Program,  
University of California, Riverside, Riverside, CA, 92521 USA*

(Dated: May 4, 2022)

# Abstract

Domain walls, topological defects that define the frontier between regions of different stacking order in multilayer graphene, have proved to host exciting physics. The ability of tuning these topological defects in-situ in an electronic transport experiment brings a wealth of possibilities in terms of fundamental understanding of domain walls as well as for electronic applications. Here, we demonstrate through a MEMS (micro-electromechanical system) actuator and magnetoresistance measurements, the effect of domain walls in multilayer graphene quantum Hall effect. Reversible and controlled uniaxial strain triggers the topological defects, manifested as new quantum Hall effect plateaus as well as a discrete and reversible modulation of the current across the device. Our findings are supported by theoretical calculations and constitute indication of the in-situ tuning of topological defects in multilayer graphene probed through electronic transport, opening the way to the use of reversible topological defects in electronic applications.

## I. INTRODUCTION

With the emergence of the field of 2D materials, strain has provided an external tunable parameter that leads to exciting physics and applications, from strain-induced gauge fields that result into enormous pseudo-magnetic fields in graphene [1, 2] to devices capable of detecting fine local deformations [3–5]. A few mechanisms have been proved successful in reversibly tuning strain in layered materials [6, 7], leading to measurable effects despite layered materials' typical large stiffness [8, 9]. An interesting predicted effect in multilayer graphene under strain is the emergence of domain walls, consequence of the applied tension not being distributed evenly across all the graphene layers [10, 11].

Domain walls also known as partial dislocations, are topological defects found at the borderline between different stacking orders in multilayer graphene and are behind intriguing phenomena. They occur naturally and they are restricted to the basal plane, which imposes an extreme boundary condition that results in confinement [12, 13]. Bilayer graphene, being the thinnest material that can host such topological defects, has revealed through transmission electron microscopy (TEM) the dynamics and patterns of these defects, that are known to behave as solitons [14]. It has been found that electronic transport along the

---

\* PA and YH contributed equally to this work.

defects occurs through valley-polarized chiral electrons [15–18]. Additionally, it is known that some configurations of partial dislocations completely block electronic transport across the dislocations while others don't have an effect, providing a possible explanation for the both observed metallic and insulating behavior in bilayer graphene at the Dirac point [19, 20].

In general, identifying the effect of topological defects in a conductance measurement is challenging. Electronic devices are usually not compatible with imaging techniques such as TEM and while it has been demonstrated that topological defects can be identified through near-field infrared nanoscopy [15], simultaneous tuning of the defects and conductance measurements remain out of reach. Additionally, because domain walls are naturally occurring in multilayer graphene, their contribution to electronic transport is usually buried within other effects such as charged impurities and other defects. Here, we use a MEMS (micro-electromechanical system) actuator to controllably create uniaxial strain in suspended multilayer graphene (6-7 layers) in a reversible and controlled manner, that in turn modifies the domain wall landscape in the multilayer graphene. Domain walls are dynamically created by uniaxial strain applied to the sample using the MEMS actuator while we simultaneously measure electronic transport at low temperature with an external magnetic field. We observe a strain-induced effect on QHE features as well as a discrete modulation of the current across the device, that we attribute to a strain-induced tuning of topological line defects in the multilayer graphene. Theoretical calculations are presented to contrast our findings.

## II. SAMPLE FABRICATION

We started with our unique MEMS chips, for which the top surfaces are polished to extremely flat faces with only a few nanometers of surface topology variation, with no deep trenches or holes in contrast with other methods [21]. Such a flat surface allows an easy transferring, patterning and electrical contacting of the multilayer graphene by nanofabrication techniques. Transfer microscopes and micromanipulators allowed to locate the multilayer graphene and transfer it into precise locations of the MEMS chips. This process is followed by nanolithography to pattern and define clamping metal electrodes and finally, the silicon dioxide sacrificial layer is etched away followed by critical point drying. The integrated 6-7 layer graphene is suspended with both ends anchored by metal supports onto a movable structure supported by flexural beams. The metal supports anchor the

multilayer graphene sample from its top surface, creating the asymmetry in tension force needed for the creation of domain walls [10, 11]. The tension forces are generated by the connected MEMS actuators which utilize electrostatic force. A scanning electron microscopy (SEM) image of the sample is shown in Figure 1. Detailed fabrication process is described in Appendix A and Supplementary Materials [22] (see also references [23–35] therein).

### III. ELECTRONIC TRANSPORT MEASUREMENTS AND THEORETICAL CALCULATIONS

Thanks to the fact that MEMS are compatible with high vacuum and cryogenic temperatures, we were able to probe strain-induced effects through electronic transport in a closed cycle cryostat with a superconducting magnet. Electronic transport measurements were performed in a temperature range of 1.5 K - 300 K and magnetic fields up to 12 T on one 6-7 layer graphene sample with a close to square geometry. Differential conductance was measured by superimposing an AC voltage ( $800 \mu\text{V}$ ) to a DC bias voltage (up to 90 mV) and measuring the current modulation by lockin detection. Similarly, differential resistance at zero bias was measured imposing an AC current (10 nA) and measuring the DC voltage drop across the sample.

Despite the fact that domain walls are present in multilayer graphene and do influence electronic transport, their contribution is difficult to discriminate. It is only through the effect of strain and continuous electronic transport measurements that the impact of such defects becomes discernible. Strain was introduced by the electrostatic actuator, where a DC voltage was applied to the MEMS actuators in the range  $0 \text{ V} - 80 \text{ V}$  to control the tension on the 6-7 layer graphene. This voltage range imposes an averaged strain level of  $0 - 0.21\%$  on the sample, as estimated through the hybrid device model detailed in Appendix B. We observed that the effect of the strain was reversible, reflected both on the sample resistance and on the features of the differential conductance and magnetoresistance, as presented later. Our finite element analysis revealed a non-uniform strain distribution where the strain at the corners of the sample is the highest, where we believe the domain walls are first triggered before traversing the sample (see Supplementary Materials [22]). As the inner layers of the multilayer graphene have no contact to the anchors, we believe that strain is applied only to the outermost layers of the 6-7 layer graphene. Molecular dynamics (MD)

simulations presented elsewhere [36] show that in the case of strained trilayer graphene, interlayer dislocations occur only between the bottom and the middle layers.

Magnetoresistance measurements are presented in Figure 2. We fixed the actuation voltage and continuously varied the magnetic field as we measured the graphene resistance at zero bias. The data was collected in the following order:  $V_{act}= 80 V, 0 V, 40 V, 60 V, 20 V$ . Data for  $V_{act} = 80 V$  was very similar to data for  $V_{act}= 60 V$ . In the same way, data for  $V_{act}= 0 V$  was very similar to  $V_{act}= 20 V$ . As will be detailed later, we believe that only  $V_{act} = 40 V$  and  $V_{act} = 60 V$  imposed a strain on the sample large enough to trigger new domain walls on the sample, discernible in the magnetoresistance measurements. Figure 2 represents only the data for  $V_{act}= 80 V, V_{act}= 40 V$  and  $V_{act}= 0 V$  for clarity. A plot of the data for all  $V_{act}$  can be found in the Supplementary Materials. It can be observed in Figure 2 an increasing tendency of the Quantum Hall Effect (QHE) features for larger voltages on the actuators despite the data not being taken in an incremental order for  $V_{act}$ . This testifies the reversibility of the strain imposed on the sample. From the data in the absence of strain ( $V_{act}=0 V$ ), we deduced the sample mobility  $\mu \approx 5000\text{cm}^2/\text{Vs}$ . This value was extracted from the lowest magnetic field value at which quantum Hall effect features are apparent (2T), corresponding to a regime where charge carriers complete individual cyclotron orbits before suffering scattering ( $\mu B \approx 1$  or  $\omega_c \tau \approx 1$ ). Using values reported in the literature for the effective mass and Fermi velocity in a 7-layer graphene  $m^*/m_e = 0.031$  [37] and  $v_F = 1.03 \times 10^6$  m/s [38] we estimated a mean free path value of  $l_e = 90$  nm, corresponding to a diffusive regime.

Because our measurements are two-probe, quantum Hall effect-like features are strongly dependant on the aspect ratio and the geometry of the sample. As reported by Abanin et al.[39, 40], multilayer graphene samples close to a square geometry ( $L \approx W$ ) present a conductance that is a monotonic function of the filling factor  $\nu$  with marked QHE plateaus, in consistency with the data for our close to square sample ( $L/W = 0.7$ ). Despite the fact that our devices lacked an electrostatic gate which precluded the tuning of the filling factor through the electronic density ( $\nu = nh/Be$ ), the equivalent effect was achieved by varying the magnetic field. As strain was imposed on the sample new features appeared at magnetic fields where QHE plateaus can be identified in the absence of strain. Our data is in qualitative agreement with the outcome of our calculations, that we develop next.

We simulated numerically the effect of a domain wall in bilayer graphene QHE, finding

new QHE plateaus that are absent if no domain walls are included. We consider a 1D domain wall on the plane of a bilayer graphene, perpendicular to the electron flow, and subject to a magnetic field perpendicular to the plane of the sample. In general, bilayer graphene is known to present an unconventional QHE, consequence of the coupling of the two graphene layers that turns graphene's Dirac Fermions into chiral quasiparticles with a quadratic dispersion relation, resulting in a characteristic Landau quantization. Figure 3 shows a schematics of the conventional integer QHE typical of a bilayer graphene. The transverse resistivity shows a plateau every time there is a filled integer number of Landau levels, determined by the filling factor  $\nu = nh/eB$ , with  $n$  the electronic density and  $h$  Planck's constant. In the bilayer graphene this corresponds to  $\nu = nh/eB = 4(N + 1)$  with  $N = 0, 1, 2, 3, \dots$ . The transverse resistivity takes the form  $\rho = (1/(N + 1))(4h/e^2)$  with  $N = 0, 1, 2, 3, \dots$  corresponding to  $\rho = (1/4)(h/e^2)$ ,  $(1/8)(h/e^2)$ ,  $(1/12)(h/e^2)$ ,  $(1/16)(h/e^2)$  etc. Interestingly, when a domain wall is added perpendicular to the electron flow, new plateaus appear at  $\rho = (1/6)(h/e^2)$ ,  $(1/10)(h/e^2)$ ,  $(1/14)(h/e^2), \dots$  as shown in Figure 3 and in consistency with another recent theoretical work [41].

The appearance of the additional plateaus can be understood from symmetry arguments. It has been demonstrated in the past that QHE in twisted bilayer graphene presents the same plateau resistance values as a commensurate Bernal bilayer, consequence of an absence of symmetry breaking [42, 43]. Here, the addition of a domain wall creates a sublattice symmetry breaking. Across the domain wall, the A and B carbon sites change places. That is, the carbon atoms that used to be sites A on one side of the domain wall, become sites B on the other side of the domain wall. Therefore, the A-B sublattice symmetry that prevents midplateaus in bilayer graphene (or two layers of a multilayer graphene) is broken once a domain wall is introduced, giving rise to midplateaus in the transverse resistivity.

We repeated the calculation for 6 layers of graphene, presented in the Supplementary Materials [22]. We found agreement with previous calculations for the transverse resistance of a 6-layer graphene [24]  $R = (1/(N + 3))(4h/e^2)$  with  $N = 0, 1, 2, 3, \dots$  corresponding to  $R = (1/12)(h/e^2)$ ,  $(1/16)(h/e^2)$ ,  $(1/20)(h/e^2)$ , etc. Plateaus have the same resistivities as those for bilayer graphene, except that the first two plateaus are shifted. Adding a domain wall introduces additional plateaus (in bold)  $R = (1/12)(h/e^2)$ ,  **$(1/14)(h/e^2)$** ,  $(1/16)(h/e^2)$ ,  **$(1/18)(h/e^2)$** ,  $(1/20)(h/e^2)$ ,  **$(1/22)(h/e^2)$** ,  $(1/24)(h/e^2)$ . This qualitatively the same as what happens in bilayer graphene, where the plateaus in the presence of a soliton take the

values (in bold the plateaus added due to the domain wall)  $R = (1/4)(h/e^2)$ ,  $(\mathbf{1/6})(h/e^2)$ ,  $(1/8)(h/e^2)$ ,  $(\mathbf{1/10})(h/e^2)$ ,  $(1/12)(h/e^2)$ ,  $(\mathbf{1/14})(h/e^2)$ ,  $(1/16)(h/e^2)$ . While the appearance of mid plateaus in the Hall resistivity in the presence of a domain wall seems to be universal, the filling factor ( $eB/nh$  values) at which they appear needs further study.

Figure 4 shows the computed difference of the calculated magnetoresistance for a bilayer graphene with and without a domain wall  $\Delta R$  (right panel) compared to the measured magnetoresistance acquired in the presence and absence of strain in the multilayer graphene (left panel). Despite the fact that we are not able to label the Landau levels, consequence of a non-functional gate voltage, we find a qualitative agreement.

We have represented in the Supplementary Materials [22] a fan diagram (Landau level index  $N$  vs  $1/B$ ) of the QHE features observed in the data both in the absence ( $V = 0$ ) and in the presence of strain ( $V = 80V$ ). In both cases, the data fits to a line as expected. Most importantly, the intercept of the fit with the y-axis for the data in the presence of strain is shifted by  $1/2$  with respect to the data in the absence of strain. This is expected from the integer sequences for the transverse resistance and the Landau level index for multilayer graphene in the absence and presence of a domain wall, as detailed in the Supplementary materials.

We now turn to the differential conductance measurements presented in Fig. 5, where we observe a discrete modulation of the current across the device as a function of strain, in consensus with reported findings using a different experimental technique. Schweizer et al. [44] have demonstrated through a dedicated scanning electron microscope setup, that partial dislocations in bilayer graphene can be manipulated to turn the sample into different topological states, as a result of recombination of the dislocation lines. By using a micromanipulator with a fine tip in-situ, they create a switching reaction that enables the connection and separation of spatially confined areas of different stacking order, that behave as topological switches, where current traveling from source to drain may encounter (or not) areas of different stacking order. We attribute the observed discrete changes of the differential conductance in our samples to be consequence of a similar effect created by strain, as we develop next.

Differential conductance measurements were taken in the following order: (1) we applied different driving voltages to the MEMS actuators to tension the sample to different strain levels; (2) at each fixed driving voltage, we applied different magnetic fields; and (3) at

each fixed magnetic field, we performed differential conductance measurements. (See supplemental materials for the complete set of data). Interestingly, the differential conductance measured for different voltages on the actuators was identical unless a magnetic field was imposed. The effect became observable at around  $1.65 T$ , close to the onset of quantum oscillations, as observed in the magnetoresistance (Figure 2). As the magnetic field increased, we noticed that the curves divided into three groups:  $\{0 V, 20 V\}$ ,  $\{40 V\}$  and  $\{60 V, 80 V\}$  (see Fig. 5). We believe that the differential conductance with no voltage on the actuators represents a starting configuration of the domain walls in the sample. As shown in Fig. 5, applying  $20 V$  doesn't impose a strong enough strain to change the domain wall landscape in the sample. Only  $40 V$  and  $60 V$  generate dislocation reactions that result into discrete changes in the conductance across the sample. We believe that these changes in the conductance are consequence of an increase of backscattering, created by the strain-induced domain walls. Indeed, the increment of backscattering is also responsible for the additional QHE plateaus observed with strain (Figs. 2 and 3), as found in our calculations and detailed in ref. 41.

The overall evolution of the features in the differential conductance near zero bias at different magnetic fields is dictated by the behavior in the absence of strain (see Figure 6) showing that the domain walls generated by strain have little effect on the phonon modes of the suspended multilayer graphene. As detailed in the Supplementary Materials [22], we have found that in the absence of strain and magnetic field, the differential conductance shows features with a periodicity of  $\approx 20 meV$  (inset of Figure 6) indicating a coupling to the lowest energy optical phonon mode in graphite, corresponding to neighboring non-equivalent planes vibrating in phase opposition along the  $c$  axis. A similar behavior for suspended multilayer graphene has been reported in [28] and [33].

#### IV. CONCLUSIONS

Through a reversible and controlled adjustment of uniaxial strain, we were able to tune the electronic transport in suspended graphene, manifested as new QHE plateaus as well as a discrete modulation of the conductance across the device, in consistency with the idea that strain creates domain walls perpendicular to the electron flow and supported by our calculations. In the absence of strain, we identified features in the differential conductance

corresponding to the coupling of an optical phonon mode in graphite, in agreement with previous works on suspended multilayer graphene. As strain was applied to the sample, we observed a discrete modulation of the differential conductance across the sample activated by strain, that we understand as the tuning of the dislocation landscape in the sample, that generates additional scattering when a new domain wall is created across the path of the electrical current.

Most importantly, our results suggest that while adding regular disorder to multilayer graphene preserves its characteristic QHE features, it is only through the addition of domain walls that the quantization of the resistivity is modified. Our work constitutes a first experimental illustration of the effect of the arrangement of multilayer graphene domain walls in the quantum Hall effect regime, and paves the way for the use of reversible topological defects for electronic applications.

## **APPENDIX A: FABRICATION PROCESS OF THE MEMS-GRAPHENE HYBRID DEVICE**

The process starts with silicon on insulator (SOI) wafers (See Figure in the Supplementary materials [22] illustrating the fabrication steps). The top silicon is first patterned to the designed structures using photolithography and deep reactive ion etching. Sacrificial silicon oxide is then filled in between the spacing of the structural silicon. Chemical-mechanical polishing is used to make a smooth top surface for graphene transferring. Thin graphene flakes are first mechanically exfoliated on a Si/SiO<sub>2</sub> substrate. The flakes with desired number of layers are identified by its optical contrast then confirmed by its distinct Raman signatures. Then the target graphene flake is transferred with a polymer support by a micromanipulator to a designated location of MEMS chips with high accuracy. Subsequently standard electron-beam lithography techniques are used to pattern graphene and define clamping metal electrodes. In the final step, the silicon dioxide sacrificial filler is etched away in 5:1 BHF, and the chips are dried with a critical point drier to acquire freestanding MEMS devices. In the resulting device, the multilayer graphene is suspended together with the structural silicon beams, because the silicon dioxide beneath has been fully etched away. The movable structural silicon beams are connected to two microactuators that can pull the graphene sample from both ends to opposite directions, controlling the displacement of the

graphene.

## APPENDIX B: MECHANICAL MODELING

The MEMS-graphene hybrid device consists of 2 comb-shape electrostatic actuators at both ends pulling the graphene flake in the middle to opposite directions. We use a lumped model to estimate the displacement of the graphene due to the actuators. At 20 V, 40 V, 60 V and 80 V, the strain of the graphene flake is estimated as 0.01%, 0.05%, 0.12% and 0.21% respectively. See Supplementary Materials for details [22].

## APPENDIX C: THEORETICAL CALCULATIONS

We computed the quantum transport through the bilayer graphene with a domain wall using the open-source computer package Kwant [45]. For that purpose we considered the bilayer graphene of the finite width of 12 nm. This width is large enough to eliminate finite-size effects. The scattering region of the bilayer graphene has a length of 7.3 nm. On each side of the bilayer graphene, the scattering region is connected to semi-infinite leads. The tight-binding model for graphene is based on Slater-Koster parameterization from Ref. [46]. Since Slater-Koster parameterization depends only on distances and angles between atoms, we can apply the same parameterization both to the region away from the domain wall, or the region near the domain wall. We applied the magnetic field to the model by using the Peierls substitution. The domain wall was modeled by shifting one of the layers of graphene by a fraction of a unit-cell vector so that on each side of the scattering region there is a continuous transition into the semi-infinite leads. The domain wall is modeled with a sigmoid function  $\frac{1}{e^{x/a}+1}$  where  $x$  is location along the bilayer and parameter  $a$  equals 0.8 nm. However, we tested that a larger domain wall-size gives qualitatively the same final result for transport. The disorder was modeled by adding a constant onsite energy shift to every carbon site. In the experiment, such energy shift can be associated to thermal fluctuations or curvature of the sample. The energy shift was chosen at random from a Gaussian distribution with a full-width-at-half-maximum of 0.3 eV. Transport was computed averaged over ten realizations of the disorder. Results using full-width-at-half-maximum of 0.1 eV and 0.6 eV gave similar results. For all disorder considered, the new quantum Hall effect (QHE)

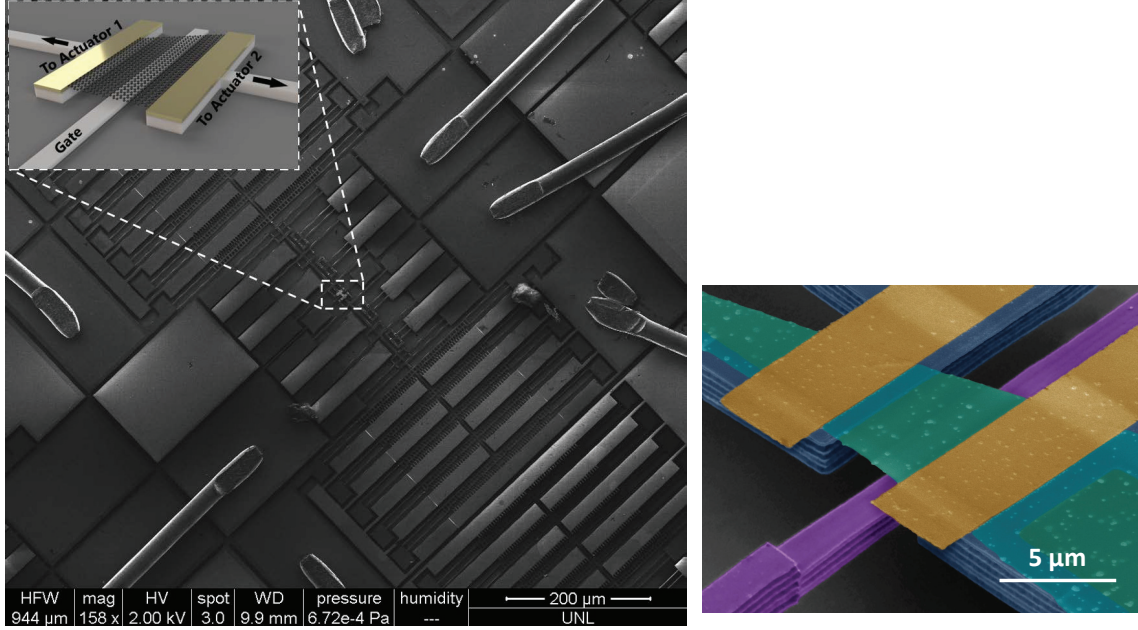


FIG. 1. **MEMS actuators and graphene.** Left: SEM image of the MEMS chip showing the suspended graphene (represented in the inset) held by movable structural silicon beams connected to the two MEMS actuators. Right: Zoom-in image of the suspended graphene (green) showing source and drain electrodes (yellow) and back gate (purple).

plateaus (associated to a domain wall added perpendicular to the electron flow) were robust and didn't disappear as disorder was increased. Disorder widens the QHE plateaus but doesn't create steps between the plateaus.

## V. ACKNOWLEDGEMENT

Funding for this work was provided by the U.S. Department of Energy, Office of Science, Office of Basic Energy Sciences under contract DE-SC0018154. S. C. was supported by the National Science Foundation, award number DMR-1848074. CO-A would like to acknowledge invaluable advice from David Warren from Oxford Instruments. We would like to acknowledge discussions as well as preliminary calculations by Gautam Rai and Stephan

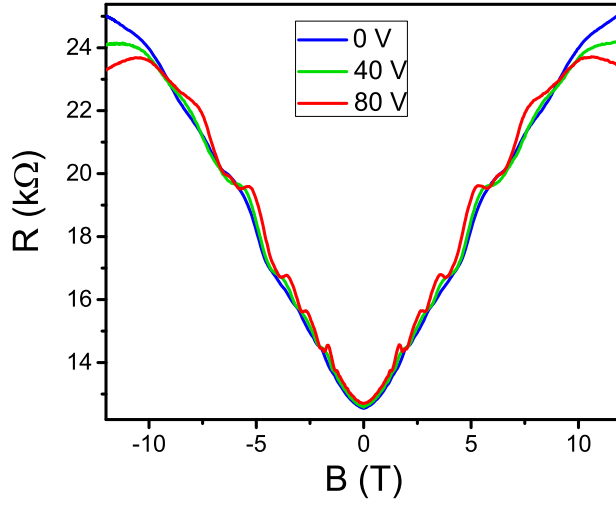


FIG. 2. **Magnetoconductance. Experiment and theory** Experimental magnetoconductance at 1.5 K for different voltages on the actuator. 0 V represents no strain and 80 V maximum strain.

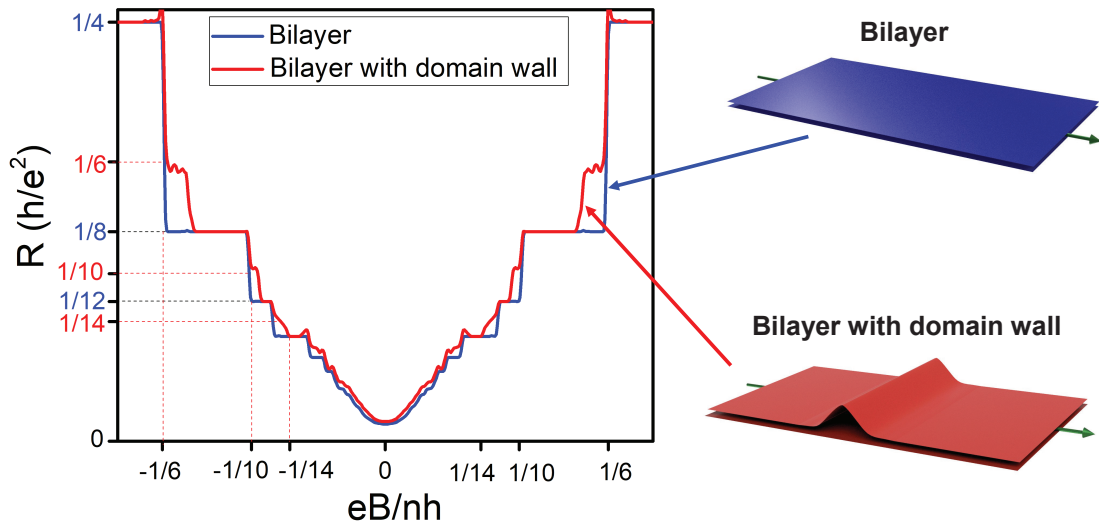


FIG. 3. **Quantum Hall resistance in bilayer graphene** is contrasted with the effect of adding a domain wall orthogonal to the electron transport. Bilayer QHE plateaus are indicated in black. Additional plateaus appear at  $(1/6)(h/e^2)$ ,  $(1/10)(h/e^2)$ ,  $(1/14)(h/e^2)$ ,  $\dots$ , marked in red. Disorder has been included in the calculations as detailed in Appendix C

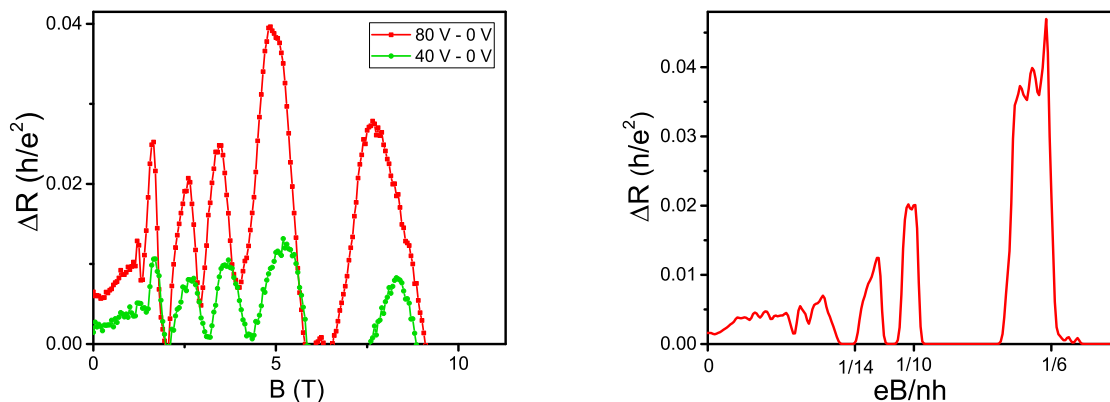


FIG. 4. **Magnetoresistance with no domain walls subtracted from the magnetoresistance with domain walls  $\Delta R$**  The experimental  $\Delta R$  (left) represents the magnetoresistance for a non-zero voltage on the actuator  $V_{Act}$  subtracted from the magnetoresistance at  $V_{Act} = 0$ . The red (green) curve corresponds to the magnetoresistance for  $V_{Act}=80$  V ( $V_{Act}=40$  V) subtracted from the magnetoresistance at  $V_{Act}=0$  V (as represented in Figure 2). The theoretically calculated  $\Delta R$  (right) represents the magnetoresistance with a domain wall subtracted from the magnetoresistance with no domain wall, as shown in Figure 3

Haas.

- 
- [1] F. Guinea, M. Katsnelson, and A. Geim, Energy gaps and a zero-field quantum hall effect in graphene by strain engineering, *Nature Physics* **6**, 30 (2010).
  - [2] N. Levy, S. Burke, K. Meaker, M. Panlasigui, A. Zettl, F. Guinea, A. C. Neto, and M. F. Crommie, Strain-induced pseudo-magnetic fields greater than 300 tesla in graphene nanobubbles, *Science* **329**, 544 (2010).
  - [3] A. Sakhaee-Pour, M. Ahmadian, and A. Vafai, Potential application of single-layered graphene sheet as strain sensor, *Solid State Communications* **147**, 336 (2008).
  - [4] S. B. Kumar and J. Guo, Strain-induced conductance modulation in graphene grain boundary, *Nano letters* **12**, 1362 (2012).
  - [5] Y. Wang, L. Wang, T. Yang, X. Li, X. Zang, M. Zhu, K. Wang, D. Wu, and H. Zhu, Wearable and highly sensitive graphene strain sensors for human motion monitoring, *Advanced*

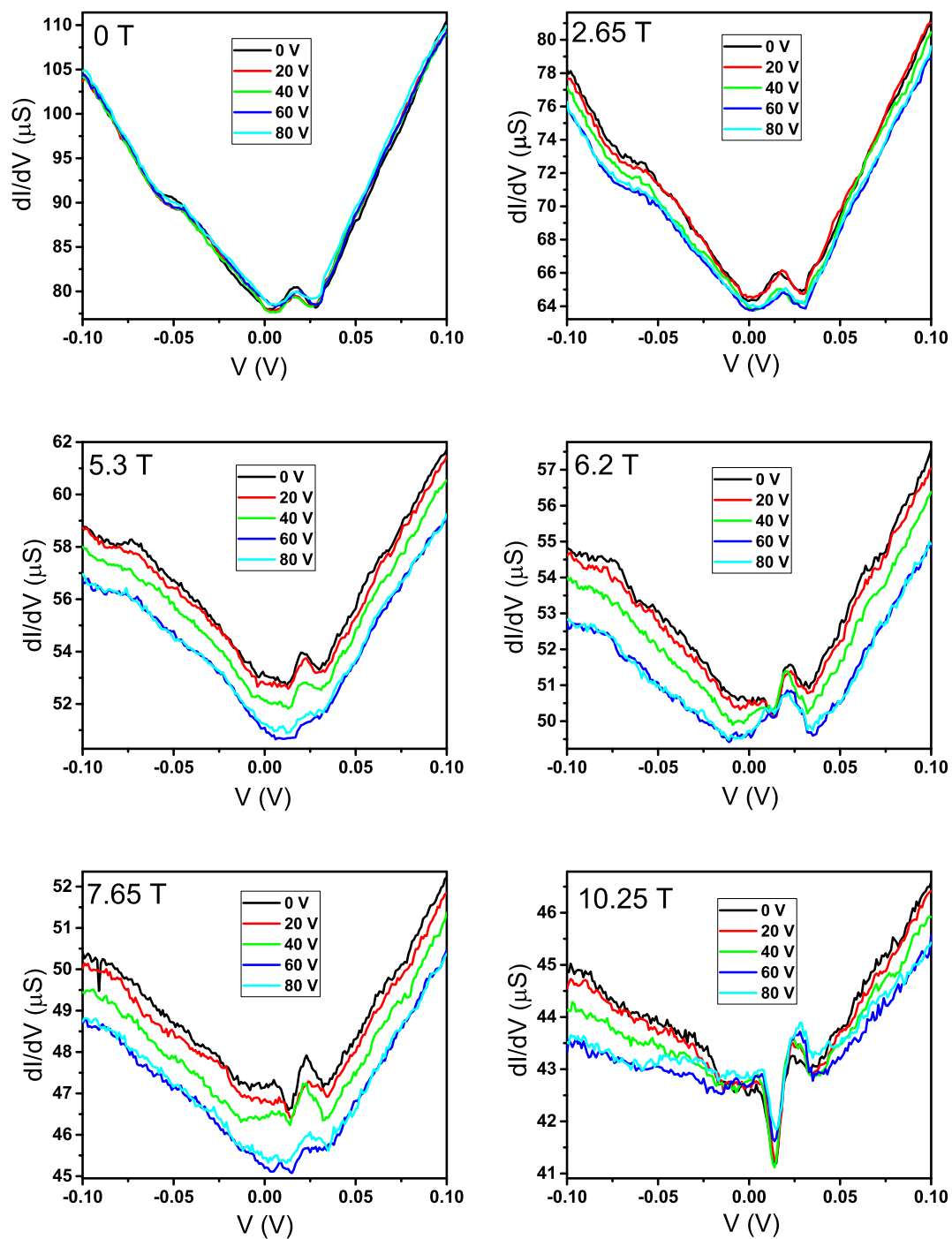


FIG. 5. Differential conductance as a function of the bias voltage for different voltages on the actuator. Each panel shows data taken at different magnetic fields (0T, 2.65T, 5.3T, 6.2T, 7.65T, 10.25T)

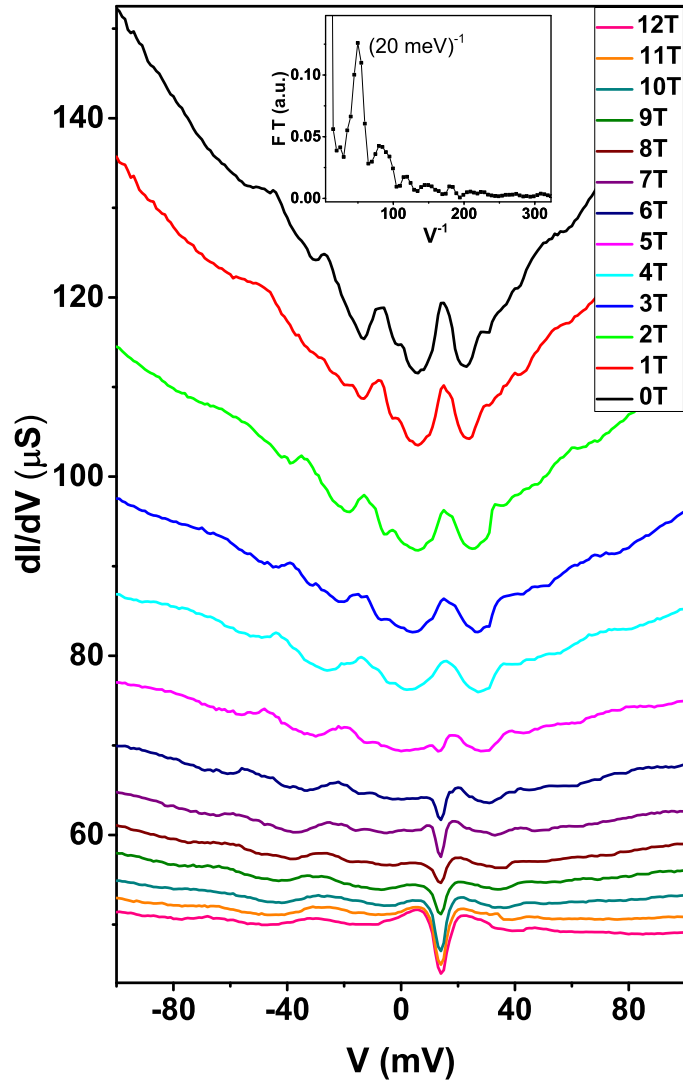


FIG. 6. Bias dependent differential conductance ( $dI/dV$ ) with no strain at different magnetic fields Range of 0T to 12T. Inset: Fourier transform of the  $dI/dV$  at 0T that indicates a periodicity of  $(20 \text{ meV})^{-1}$

Functional Materials **24**, 4666 (2014).

- [6] H. H. Perez Garza, E. W. Kievit, G. F. Schneider, and U. Staufer, Controlled, reversible, and nondestructive generation of uniaxial extreme strains in graphene, Nano letters **14**, 4107 (2014).

- [7] J. H. Hinnefeld, S. T. Gill, S. Zhu, W. J. Swanson, T. Li, and N. Mason, Reversible mechanical and electrical properties of ripped graphene, *Physical Review Applied* **3**, 014010 (2015).
- [8] C. Lee, X. Wei, J. W. Kysar, and J. Hone, Measurement of the elastic properties and intrinsic strength of monolayer graphene, *science* **321**, 385 (2008).
- [9] S. Bertolazzi, J. Brivio, and A. Kis, Stretching and breaking of ultrathin mos2, *ACS nano* **5**, 9703 (2011).
- [10] H. Kumar, L. Dong, and V. B. Shenoy, Limits of coherency and strain transfer in flexible 2d van der waals heterostructures: formation of strain solitons and interlayer debonding, *Scientific reports* **6**, 1 (2016).
- [11] L. Yang, H. Xu, K. Liu, D. Gao, Y. Huang, Q. Zhou, and Z. Wu, Molecular dynamics simulation on the formation and development of interlayer dislocations in bilayer graphene, *Nanotechnology* **31**, 125704 (2020).
- [12] S. Amelinckx, et delavignette, p, *Nature* **185**, 603 (1960).
- [13] B. Butz, C. Dolle, F. Niekiel, K. Weber, D. Waldmann, H. B. Weber, B. Meyer, and E. Spiecker, Dislocations in bilayer graphene, *Nature* **505**, 533 (2014).
- [14] J. S. Alden, A. W. Tsen, P. Y. Huang, R. Hovden, L. Brown, J. Park, D. A. Muller, and P. L. McEuen, Strain solitons and topological defects in bilayer graphene, *Proceedings of the National Academy of Sciences* **110**, 11256 (2013).
- [15] L. Ju, Z. Shi, N. Nair, Y. Lv, C. Jin, J. Velasco, C. Ojeda-Aristizabal, H. A. Bechtel, M. C. Martin, A. Zettl, *et al.*, Topological valley transport at bilayer graphene domain walls, *Nature* **520**, 650 (2015).
- [16] I. Martin, Y. M. Blanter, and A. Morpurgo, Topological confinement in bilayer graphene, *Physical review letters* **100**, 036804 (2008).
- [17] F. Zhang, A. H. MacDonald, and E. J. Mele, Valley chern numbers and boundary modes in gapped bilayer graphene, *Proceedings of the National Academy of Sciences* **110**, 10546 (2013).
- [18] A. Vaezi, Y. Liang, D. H. Ngai, L. Yang, and E.-A. Kim, Topological edge states at a tilt boundary in gated multilayer graphene, *Physical Review X* **3**, 021018 (2013).
- [19] P. San-Jose, R. Gorbachev, A. Geim, K. Novoselov, and F. Guinea, Stacking boundaries and transport in bilayer graphene, *Nano letters* **14**, 2052 (2014).
- [20] S. Shallcross, S. Sharma, and H. B. Weber, Anomalous dirac point transport due to extended defects in bilayer graphene, *Nature communications* **8**, 1 (2017).

- [21] R. A. Bernal, A. Aghaei, S. Lee, S. Ryu, K. Sohn, J. Huang, W. Cai, and H. Espinosa, Intrinsic bauschinger effect and recoverable plasticity in pentatwinned silver nanowires tested in tension, *Nano letters* **15**, 139 (2015).
- [22] See Supplemental Material at [URL will be inserted by publisher] for schematics of the device fabrication, details on the mechanical modeling of the MEMS-graphene hybrid device, Raman data of the measured device, a finite element analysis to estimate the strain distribution in the graphene flake, a discussion of the measurements on the suspended multilayer graphene in the absence of strain and a full set of data for the differential conductance of the multilayer graphene in the presence of strain.
- [23] H. Li, J. Wu, X. Huang, G. Lu, J. Yang, X. Lu, Q. Xiong, and H. Zhang, Rapid and reliable thickness identification of two-dimensional nanosheets using optical microscopy, *ACS nano* **7**, 10344 (2013).
- [24] H. Min and A. H. MacDonald, Chiral decomposition in the electronic structure of graphene multilayers, *Phys. Rev. B* **77**, 155416 (2008).
- [25] Y. Cao, V. Fatemi, S. Fang, K. Watanabe, T. Taniguchi, E. Kaxiras, and P. Jarillo-Herrero, Unconventional superconductivity in magic-angle graphene superlattices, *Nature* **556**, 43 (2018).
- [26] A. C. Neto, F. Guinea, N. M. Peres, K. S. Novoselov, and A. K. Geim, The electronic properties of graphene, *Reviews of modern physics* **81**, 109 (2009).
- [27] G.-L. Ingold and Y. V. Nazarov, Charge tunneling rates in ultrasmall junctions, in *Single charge tunneling* (Springer, 1992) pp. 21–107.
- [28] A. Chepelianskii, P. Delplace, A. Shailos, A. Kasumov, R. Deblock, M. Monteverde, C. Ojeda-Aristizabal, M. Ferrier, S. Guéron, and H. Bouchiat, Phonon-assisted dynamical coulomb blockade in a thin suspended graphite sheet, *Physical Review B* **79**, 235418 (2009).
- [29] A. Bachtold, M. De Jonge, K. Grove-Rasmussen, P. McEuen, M. Buitelaar, and C. Schönberger, Suppression of tunneling into multiwall carbon nanotubes, *Physical review letters* **87**, 166801 (2001).
- [30] M. Bockrath, D. H. Cobden, J. Lu, A. G. Rinzler, R. E. Smalley, L. Balents, and P. L. McEuen, Luttinger-liquid behaviour in carbon nanotubes, *Nature* **397**, 598 (1999).
- [31] B. Altshuler and A. Aronov, Zero bias anomaly in tunnel resistance and electron—electron interaction, *Solid State Communications* **88**, 1033 (1993).

- [32] Y. Imry and Z. Ovadyahu, Density-of-states anomalies in a disordered conductor: a tunneling study, *Physical Review Letters* **49**, 841 (1982).
- [33] S. Lee, N. Wijesinghe, C. Diaz-Pinto, and H. Peng, Hot electron transport in suspended multilayer graphene, *Phys. Rev. B* **82**, 045411 (2010).
- [34] L. Vitali, M. Schneider, K. Kern, L. Wirtz, and A. Rubio, Phonon and plasmon excitation in inelastic electron tunneling spectroscopy of graphite, *Physical Review B* **69**, 121414 (2004).
- [35] L. Wirtz and A. Rubio, The phonon dispersion of graphite revisited, *Solid State Communications* **131**, 141 (2004).
- [36] Y. Huang, , L. Yang, K. Liu, Z. Wu, and Q. Zhou, Dislocation induced energy dissipation in tunable multilayer graphene resonators, arXiv:2108.11002.
- [37] A. AlZahrani and G. Srivastava, enGraphene to graphite: electronic changes within DFT calculations, *Brazilian Journal of Physics* **39**, 694 (2009).
- [38] M. L. Sadowski, G. Martinez, M. Potemski, C. Berger, and W. A. de Heer, Landau level spectroscopy of ultrathin graphite layers, *Phys. Rev. Lett.* **97**, 266405 (2006).
- [39] D. A. Abanin and L. S. Levitov, Conformal invariance and shape-dependent conductance of graphene samples, *Physical Review B* **78**, 035416 (2008).
- [40] J. R. Williams, D. A. Abanin, L. DiCarlo, L. S. Levitov, and C. M. Marcus, Quantum hall conductance of two-terminal graphene devices, *Physical Review B* **80**, 045408 (2009).
- [41] N. S. Bäbler and K. P. Schmidt, Effects of domain walls in bilayer graphene in an external magnetic field, arXiv preprint arXiv:2009.06315 (2020), after completion of this work we became aware of the preprint by Nico S. Babler and Kai Phillip Schmidt that studies numerically the QHE conductance in bilayer graphene, reporting the appearance of additional plateaus at integer multiples of the conductance quantum when a domain wall is introduced, supporting our findings.
- [42] D. S. Lee, C. Riedl, T. Beringer, A. C. Neto, K. von Klitzing, U. Starke, and J. H. Smet, Quantum hall effect in twisted bilayer graphene, *Physical review letters* **107**, 216602 (2011).
- [43] M. Mucha-Kruczyński, I. L. Aleiner, and V. I. Fal’ko, Strained bilayer graphene: Band structure topology and landau level spectrum, *Physical Review B* **84**, 041404 (2011).
- [44] P. Schweizer, C. Dolle, and E. Spiecker, In situ manipulation and switching of dislocations in bilayer graphene, *Science advances* **4**, eaat4712 (2018).

- [45] C. W. Groth, M. Wimmer, A. R. Akhmerov, and X. Waintal, Kwant: a software package for quantum transport, *New Journal of Physics* **16**, 063065 (2014).
- [46] G. Trambly de Laissardière, D. Mayou, and L. Magaud, Localization of dirac electrons in rotated graphene bilayers, *Nano letters* **10**, 804 (2010).

# Strain-tuning of domain walls in multilayer graphene probed in the quantum Hall regime Supplementary Materials

Paul Anderson,<sup>1</sup> Yifan Huang,<sup>2</sup> Yuanjun Fan,<sup>2</sup> Sara Qubbaj,<sup>1</sup>

Sinisa Coh,<sup>3</sup> Qin Zhou,<sup>2</sup> and Claudia Ojeda-Aristizabal<sup>1</sup>

<sup>1</sup>*Department of Physics and Astronomy,  
California State University Long Beach,  
Long Beach, California 90840, USA\**

<sup>2</sup>*Department of Mechanical and Materials Engineering,  
University of Nebraska, Lincoln 68588-0526, Nebraska, USA\**

<sup>3</sup>*Department of Mechanical Engineering and Materials Science and Engineering Program,  
University of California, Riverside, Riverside, CA, 92521 USA*

(Dated: May 4, 2022)

## I. FABRICATION STEPS OF THE DEVICE

See Figure 1 for the device fabrication steps described in the Methods section of the main text.

## II. MECHANICAL MODELING

Figure 2a shows the MEMS-graphene hybrid device as described in the Methods section of the main text. A lumped model is used to estimate the displacement of the graphene. When the two identical actuators are working at the same actuation voltage the system can be simplified as shown in Figure 2b.

The compatibility of deformation and equilibrium of the system lead to the following equations:

$$\begin{aligned} F &= k_a X_a + k_G X_G \\ 2X_a &= X_G, \end{aligned}$$

where  $F$  is the force generated by the electrostatic actuators,  $k_a$  and  $k_G$  are the spring constant of the actuator and graphene flake respectively,  $X_a$  and  $X_G$  are the displacement of the actuator and graphene respectively. The spring constant of graphene and actuator are given by:

$$\begin{aligned} k_G &= \frac{E_G A_G}{L_G} \\ k_a &= \frac{2E_a b^3 h}{L_a^3}, \end{aligned}$$

where  $E$  is young's modulus,  $A$  is the cross section area,  $b$  is width,  $h$  is thickness and  $L$  is length. The force generated by the electrostatic actuators is calculated as

$$F = \frac{n\epsilon_0 b}{d} V^2, \quad (1)$$

where  $n$  is the number of comb figures in the electrostatic actuator,  $\epsilon_0$  is dielectric constant,  $d$  is the gap spacing between the fingers,  $V$  is the actuation voltage. By solving the equations above, the actuation voltage – strain relation is found, as shown in Figure 2c). At 20 V, 40 V, 60 V and 80 V, the strain of the graphene flake is estimated as 0.01%, 0.05%, 0.12% and 0.21% respectively.

---

\* PA and YH contributed equally to this work.

### III. STRAIN DISTRIBUTION IN THE MULTILAYER GRAPHENE SAMPLE

Because the shape of graphene is an acute trapezoid (see Figure 2 in main text), the strain distribution will not be uniform. We performed a finite element analysis to simulate the strain distribution of graphene using COMSOL. As shown in Figure 3, when the actuation voltage is at 40V, even though the average strain is small, we can clearly see strain concentration at the corners, which we believe are the places where dislocations are triggered first.

### IV. RECOGNIZING THE NUMBER OF LAYERS OF THE MULTILAYER GRAPHENE IN THE MEMS DEVICE

A library of graphene flakes with different layer numbers on 300nm SiO<sub>2</sub> substrate identified by optical contrast is established using the approach described in literature [1]. Raman spectra of these samples are taken using a 488nm laser to build a standard library, and used as another approach to identify the layer number. The 2D peak is used for characterization. A reference sample is characterized as a tri-layer and our sample is estimated as 6-7 layer (see Figure 4).

### V. CALCULATIONS OF THE QUANTUM HALL RESISTANCE IN BILAYER GRAPHENE WITH NO DISORDER CONTRASTED WITH THE EFFECT OF ADDING A DOMAIN WALL

Figure 5 shows the outcome of the calculations for the magnetoresistance in bilayer graphene both with and without a domain wall orthogonal to the electron transport, similar to Figure 3 of the main text, but with no disorder included.

### VI. CALCULATION OF THE QUANTUM HALL RESISTANCE FOR 6-LAYER GRAPHENE

Figure 6 shows the outcome of the calculations for 6-layer graphene. As mentioned in the main text, the steps in the resistance show agreement with previous works [2]. We expect that adding a domain wall introduces mid-plateaus (in bold)  $R = (1/12)(h/e^2)$ ,

$(\mathbf{1/14})(h/e^2)$ ,  $(1/16)(h/e^2)$ ,  $(\mathbf{1/18})(h/e^2)$ ,  $(1/20)(h/e^2)$ ,  $(\mathbf{1/22})(h/e^2)$ ,  $(1/24)(h/e^2)$ . As shown in Figure 6, the mid plateaus are better resolved at high fields, where the effect of disorder in the calculation is less pronounced. The effect of the domain wall in the magnetoresistance is the same as in bilayer graphene, where the presence of a domain wall adds mid-steps in the resistance (in bold)  $R = (1/4)(h/e^2)$ ,  $(\mathbf{1/6})(h/e^2)$ ,  $(1/8)(h/e^2)$ ,  $(\mathbf{1/10})(h/e^2)$ ,  $(1/12)(h/e^2)$ ,  $(\mathbf{1/14})(h/e^2)$ ,  $(1/16)(h/e^2)$ . When adding more layers in the calculation (as in the case of 6-layer graphene), the results become more sensitive to the finite-size effects used in the calculation, which increases numerical noise. While the appearance of midsteps in the quantum Hall resistance as a consequence of the addition of a domain wall seems to be universal in multilayer graphene, the filling factor at which such plateaus appear needs further study.

## VII. FAN DIAGRAM OF THE OBSERVED QUANTUM HALL EFFECT FEATURES

Because we get qualitatively the same results for 2-layer and 6-layer graphene (the appearance of mid-level plateaus), representing the index of the  $0^{th}$  Landau level subtracted from the Landau level index  $N$  yields a result that is trivially independent of the number of layers.

Figure 7 shows the fan diagram for the quantum Hall effect (QHE) features that are visible both in the absence and in the presence of strain, as well the mid-QHE features that appear as a consequence of a domain wall triggered by strain. All QHE features are identified by plotting the derivative of the magnetoresistance, as illustrated in figure 8.

The relation between the Landau level index and the inverse of the magnetic field is given as follows:

*a. Bilayer graphene*

$$R_{xy}^{-1} = \frac{4e^2}{h}, \frac{8e^2}{h}, \frac{12e^2}{h}, \frac{16e^2}{h}, \dots = 4(N + 1) \frac{e^2}{h}$$

with the filling factor  $\nu$  given by

$$\nu = \frac{nh}{eB} = 4(N + 1)$$

and the Landau level index by

$$N = \frac{nh}{4eB} - 1 \tag{2}$$

In the presence of a domain wall, our calculations indicate

$$R_{xy}^{-1} = \frac{6e^2}{h}, \frac{10e^2}{h}, \frac{14e^2}{h}, \frac{18e^2}{h}, \dots = 4\left(N + \frac{3}{2}\right) \frac{e^2}{h}$$

$$\nu = \frac{nh}{eB} = 4\left(N + \frac{3}{2}\right)$$

and

$$N = \frac{nh}{4eB} - \frac{3}{2} \quad (3)$$

As cited in the main text, in general the Hall conductivity for a M-layer stack of graphene layers has plateaus conductivities of the form

$$\sigma_{xy} = \pm \frac{4e^2}{h} \left( \frac{M}{2} + N \right)$$

where N is a non-negative number [2]. Despite the fact that there are at times a dependence on the stacking order (as it is the case for trilayer graphene [3]) plateaus at  $\sigma_{xy} = (4e^2/h)(M/2)$  are in general strong in most stacks, consequence of the topological character of quantum Hall effect [2]. The quantum Hall plateaus for 6-layer graphene are therefore very similar to those for bilayer graphene, except that the first two plateaus  $4e^2/h$  and  $8e^2/h$  are shifted.

*b. 6-layer graphene*

$$R_{xy}^{-1} = \frac{12e^2}{h}, \frac{16e^2}{h}, \frac{20e^2}{h}, \frac{24e^2}{h}, \dots = 4(N + 3) \frac{e^2}{h}$$

with the filling factor  $\nu$  given by

$$\nu = \frac{nh}{eB} = 4(N + 3)$$

and the Landau level index by

$$N = \frac{nh}{4eB} - 3 \quad (4)$$

In the presence of a domain wall, our calculations indicate

$$R_{xy}^{-1} = \frac{14e^2}{h}, \frac{18e^2}{h}, \frac{22e^2}{h}, \dots = 4\left(N + \frac{7}{2}\right) \frac{e^2}{h}$$

$$\nu = \frac{nh}{eB} = 4\left(N + \frac{7}{2}\right)$$

and

$$N = \frac{nh}{4eB} - \frac{7}{2} \quad (5)$$

Comparing expressions 3, 2 with 5 and 4 it can be deduced that there is a difference of  $1/2$  between the expression for the Landau level index for no domain wall and the expression with domain wall. This difference should be observed at the intercept with the y-axis when plotting the Landau level index  $N$  vs  $1/B$  and should be independent of the labeling of the Landau levels and the number of layers.

Figure 7 shows the Landau level index  $N - N_0$  (where  $N_0$  is the lowest Landau level observed) as a function of  $1/B$ . A fit to the data corresponding to the mid-plateaus (data under strain) shows an intercept with the y-axis shifted by  $\frac{1}{2}$  with respect to the fit of the equivalent data for the plateaus (data with no strain). From both curves we deduce an electronic density of  $12 \times 10^{12}/\text{cm}^2$ .

The observed y-axis intercepts of the fit on both set of data are in accordance to what our theory predicts for quantum Hall effect in the presence of a domain wall.

### VIII. DIFFERENTIAL CONDUCTANCE WITH NO STRAIN

In the following, we present results in the absence of strain or magnetic field. The bias dependent differential conductance revealed a V shape, related to the linear density of states in graphene [4]. Typically, access to the density of states through electronic transport is granted by tunnel contacts. In our sample, transmission of the electrodes lead to an intermediate tunneling regime that can be understood through the physics of dynamical Coulomb blockade. In dynamical Coulomb blockade, tunneling takes place through a small capacitance formed at the electrodes in series with an ohmic electromagnetic environment (the graphene foils) that exchanges energy with the tunneling quasiparticles, on a scale that is significantly smaller than the charging energy of the tunneling capacitors [5]. In this Coulomb blockade regime, the differential conductance follows a scaling behavior as a function of the temperature  $T$  and bias voltage  $V$  [5, 6] as shown below

$$dI/dV = T^z f(eV/k_B T) \tag{6}$$

where  $\lim_{x \rightarrow 0} f(x) = C$ ,  $C$  is a constant and  $\lim_{x \rightarrow \infty} f(x) = x^z$ . Figure 9 shows the temperature dependence of the conductance as well as the bias dependence for our sample (shown in the main text at 1.5 K), represented in a double logarithmic scale. The exponent found ( $z = 0.19$ ) is similar to values reported for multiwall carbon nanotubes [7, 8] and suspended

multilayer graphene with low conductance contacts [6]. The differential conductance presented additionally an anomaly at zero bias. Zero bias anomalies have been associated in tunneling experiments to an interplay of electronic correlations and disorder [9, 10]. Here, we observe replica of the zero-bias feature at multiples of  $\approx 20 \text{ meV}$ , as seen in Figure 6 of the main text for  $B = 0$  (black curve). Such behavior has been reported before in suspended multilayer graphene [6, 11] where dynamical Coulomb blockade also played an important role. The periodicity of the anomalies in our data is confirmed by Fourier transform and shown as an inset in Figure 6 of the main text. Following ref. [6], we associate these features to replica of the Coulomb blockade anomaly, consequence of the coupling of the dissipating electromagnetic environment to the lowest energy optical phonon mode in graphite (ZO') [12, 13] that results into an oscillating transmission of the barriers at the contacts [6]. The ZO' optical phonon mode in graphite emerges from the out-of-plane acoustic phonon mode in graphene (ZA) [13] and corresponds to neighboring non-equivalent planes vibrating in phase opposition along the  $c$  axis [6]. The similarity between the graphite phonon mode observed here and the one reported in ref. [6] is likely related to the comparable aspect ratios of the samples ( $L < W$ ). The impact of the samples' aspect ratio is also revealed in the magnetoresistance data, as detailed in the main text.

Features in the differential conductance were highly influenced by the presence of a vertical magnetic field, as observed in Figure 6 of the main text. Replica of the zero bias anomaly evolved into a single dip at high enough fields ( $\approx 5 \text{ T}$ ). A similar effect was observed in ref. [6] and attributed to the field-dependent density of states in the multilayer graphene. The periodicity of the features ( $20 \text{ meV}$ ) has a characteristic frequency  $\omega_o$  comparable to graphene's cyclotron frequency at  $1 \text{ T}$ , assuming that the Fermi energy is near the Dirac point.

Thermal cycling created a non-negligible effect on the differential conductance features. Following the measurements shown in Figure 6 of the main text, the sample went through a thermal cycle (to room temperature and back to  $1.5 \text{ K}$ , as shown in Fig. 9) and a cycling of the voltage imposed on the actuators ( $0 \text{ V}$  to  $80 \text{ V}$ ). Impact of these experiments is found by comparing the data in Figure 6 of the main text for  $B = 0 \text{ T}$  and the first panel in Figure 13 here, where the differential conductance taken under similar conditions is represented. While there are similar features, some of the zero bias replica have been lost.

## IX. TEMPERATURE DEPENDENCE OF THE RESISTANCE

The temperature dependence of the resistance in the absence of strain was smooth (Figure 10). Fluctuations of the resistance of  $\approx 200\Omega$  were registered at  $\approx 3.4K$  as shown in the inset, likely due to the cryostat staying at that temperature for a longer amount of time during the measurement. Figure 10 shows as well the magnetoresistance for no voltage applied to the actuators ( $V_{act} = 0V$ ) for different temperatures (1.5 K, 10 K and 20 K). It can be observed that the quantum Hall effect features present at 1.5 K disappear for higher temperatures as expected.

## X. STABILITY OF THE SAMPLE AFTER AND DURING STRAIN

When the strain on the sample was retained for more than 24 hours (needed for each magnetoresistance measurement), the sample's resistance was stable. The magnetoresistance data for all voltages on the actuator retraced perfectly after the measurement was run again. A representative set of data ( $V_{act} = 80$  V) is shown in Figure 11.

From the magnetoresistance measurements at different strain (i. e. different voltage on the actuators), we extracted the resistance at zero bias and zero magnetic field (see Figure 11). Values fluctuated in a range  $900\Omega$  (about 7% of the sample's resistance). This is certainly consequence of a small deterioration of the electrical contact to the multilayer graphene after the strain was released from the sample. Magnetoresistance measurements were taken in the following order:  $V_{Act}=80$  V, 0 V, 40 V, 60 V, 20 V. The fact that the quantum Hall effect features in the magnetoresistance changed consistently for larger voltages applied to the actuators despite the data not taken in incremental order for  $V_{Act}$ , testifies the reversibility of the effect.

These observations show that the anchor and electrical contact to the multilayer graphene sample was robust during the strain experiments.

## XI. MAGNETORESISTANCE FOR ALL VOLTAGES ON THE ACTUATORS

As mentioned in the previous section, magnetoresistance was measured for different voltages on the actuators in the following order:  $V_{Act}=80$  V, 0 V, 40 V, 60 V, 20 V. Figure 12 shows the magnetoresistance for all the voltages on the actuator. It can be observed that

the relative size of the quantum Hall effect features in the data increases for larger voltages on the actuators despite the data not being taken in incremental order. Also, it can be observed that the magnetoresistance data at  $V_{Act} = 60 V$  is very similar to the magnetoresistance at  $V_{Act} = 80 V$ . In the same way, the magnetoresistance at  $V_{Act} = 0 V$  is very similar to the one at  $V_{Act} = 20 V$ . The similar magnetoresistance for  $V_{Act} = 0, 20 V$  and  $V_{Act} = 60, 80 V$  respectively is in consistency with the behavior observed for the differential conductance at  $V_{Act} = 0 V, 20 V, 40 V, 60 V$  and  $80 V$ . As explained in the main text, the differential conductance for different voltages on the actuators divided into three groups:  $\{0 V, 20 V\}$ ,  $\{40 V\}$  and  $\{60 V, 80 V\}$ . As detailed in the main text, we believe that applying 40 V and 60 V on the actuators creates a strain large enough to create new domain walls in the sample, which results into new quantum Hall plateaus discernible in two probe magnetoresistance measurements and other features discerned in the differential conductance. In contrast, the strain created by  $V_{Act} = 20 V$  and  $V_{Act} = 80 V$  is not large enough with respect to  $V_{Act} = 0 V$  and  $V_{Act} = 60 V$  respectively to create new domain walls. The magnetoresistance and differential conductance looks therefore the same for  $V_{Act} = 0, 20 V$  and  $V_{Act} = 60, 80 V$ .

## **XII. EFFECTS OF STRAIN ON DIFFERENTIAL CONDUCTANCE MEASUREMENTS**

Fig. 13 presents the whole set of data of differential conductance for different voltages imposed on the actuators taken at different magnetic fields. A switching effect of the current across the sample occurs between  $1.25 T$  and  $1.65 T$ .

## **XIII. ACKNOWLEDGEMENT**

Funding for this work was provided by the U.S. Department of Energy, Office of Science, Office of Basic Energy Sciences under contract DE-SC0018154. S. C. was supported by the National Science Foundation, award number DMR-1848074. CO-A would like to acknowledge invaluable advice from David Warren from Oxford Instruments. We would like to acknowledge discussions as well as preliminary calculations by Gautam Rai and Stephan

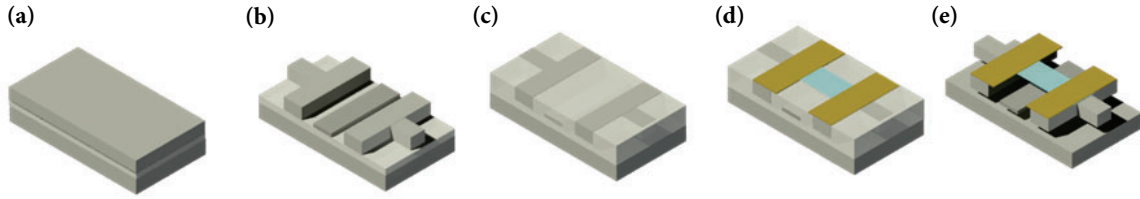


FIG. 1. **Device fabrication steps.** (a) Starting SOI wafer. (b) The top silicon is patterned using photolithography and deep reactive ion etching. (c) Sacrificial silicon oxide is filled between the spacing of the structural silicon. (d) Graphene is transferred with a polymer support and micro-manipulators to the MEMS chip. Ebeam lithography is used to define sampling metal electrodes. (e) The silicon dioxide sacrificial filler is etched away resulting in a suspended graphene sample with suspended movable silicon beams, that are connected to microactuators capable of pulling the graphene sample from both ends to opposite directions

Haas.

- 
- [1] H. Li, J. Wu, X. Huang, G. Lu, J. Yang, X. Lu, Q. Xiong, and H. Zhang, Rapid and reliable thickness identification of two-dimensional nanosheets using optical microscopy, *ACS nano* **7**, 10344 (2013).
  - [2] H. Min and A. H. MacDonald, Chiral decomposition in the electronic structure of graphene multilayers, *Phys. Rev. B* **77**, 155416 (2008).
  - [3] Y. Cao, V. Fatemi, S. Fang, K. Watanabe, T. Taniguchi, E. Kaxiras, and P. Jarillo-Herrero, Unconventional superconductivity in magic-angle graphene superlattices, *Nature* **556**, 43.
  - [4] A. C. Neto, F. Guinea, N. M. Peres, K. S. Novoselov, and A. K. Geim, The electronic properties of graphene, *Reviews of modern physics* **81**, 109 (2009).
  - [5] G.-L. Ingold and Y. V. Nazarov, Charge tunneling rates in ultrasmall junctions, in *Single charge tunneling* (Springer, 1992) pp. 21–107.
  - [6] A. Chepelianskii, P. Delplace, A. Shailos, A. Kasumov, R. Deblock, M. Monteverde, C. Ojeda-Aristizabal, M. Ferrier, S. Guéron, and H. Bouchiat, Phonon-assisted dynamical coulomb blockade in a thin suspended graphite sheet, *Physical Review B* **79**, 235418 (2009).

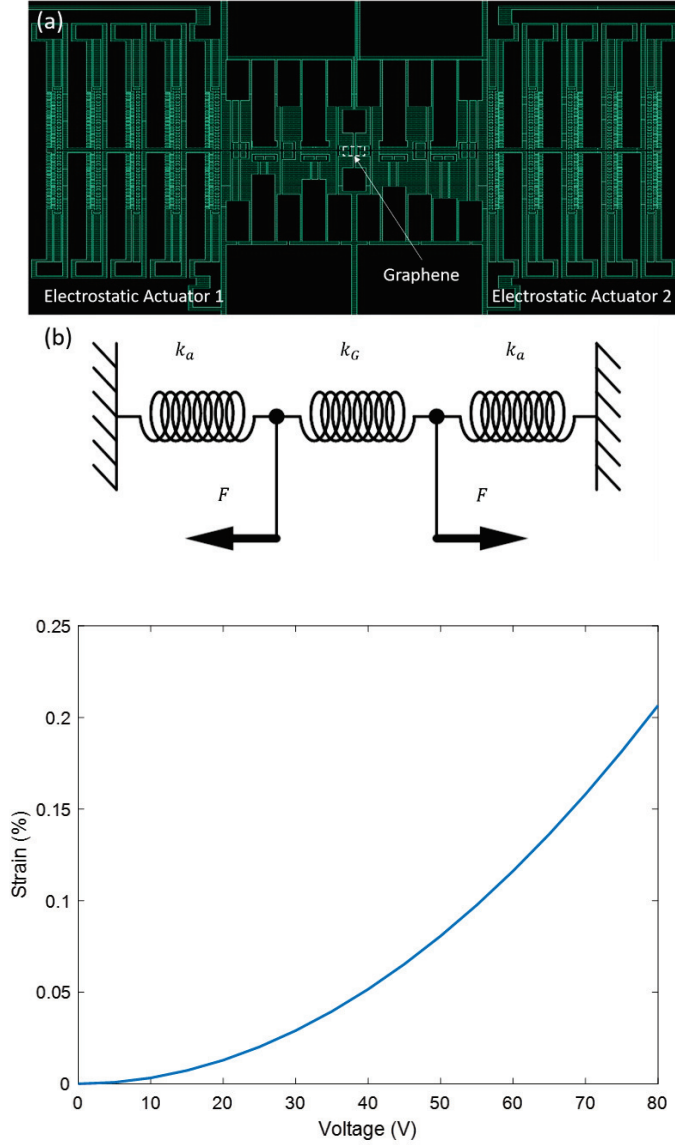


FIG. 2. **Schematic of MEMS-graphene hybrid device.** (a) Layout of the system. (b) Lumped mechanical model. (c) Actuation voltage - strain relation of the graphene sample

- [7] A. Bachtold, M. De Jonge, K. Grove-Rasmussen, P. McEuen, M. Buitelaar, and C. Schönberger, Suppression of tunneling into multiwall carbon nanotubes, *Physical review letters* **87**, 166801 (2001).
- [8] M. Bockrath, D. H. Cobden, J. Lu, A. G. Rinzler, R. E. Smalley, L. Balents, and P. L. McEuen, Luttinger-liquid behaviour in carbon nanotubes, *Nature* **397**, 598 (1999).
- [9] B. Altshuler and A. Aronov, Zero bias anomaly in tunnel resistance and electron—electron interaction, *Solid State Communications* **88**, 1033 (1993).

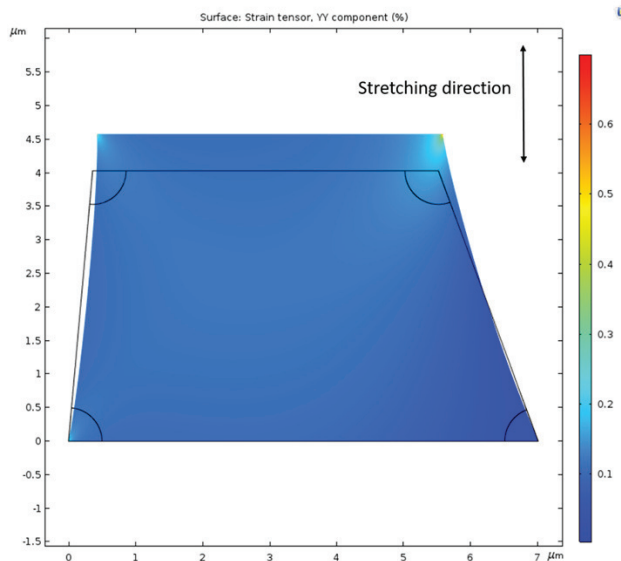


FIG. 3. Finite element analysis of strain distribution of the graphene sample 1 under uniaxial tension.

- [10] Y. Imry and Z. Ovadyahu, Density-of-states anomalies in a disordered conductor: a tunneling study, *Physical Review Letters* **49**, 841 (1982).
- [11] S. Lee, N. Wijesinghe, C. Diaz-Pinto, and H. Peng, Hot electron transport in suspended multilayer graphene, *Phys. Rev. B* **82**, 045411 (2010).
- [12] L. Vitali, M. Schneider, K. Kern, L. Wirtz, and A. Rubio, Phonon and plasmon excitation in inelastic electron tunneling spectroscopy of graphite, *Physical Review B* **69**, 121414 (2004).
- [13] L. Wirtz and A. Rubio, The phonon dispersion of graphite revisited, *Solid State Communications* **131**, 141 (2004).

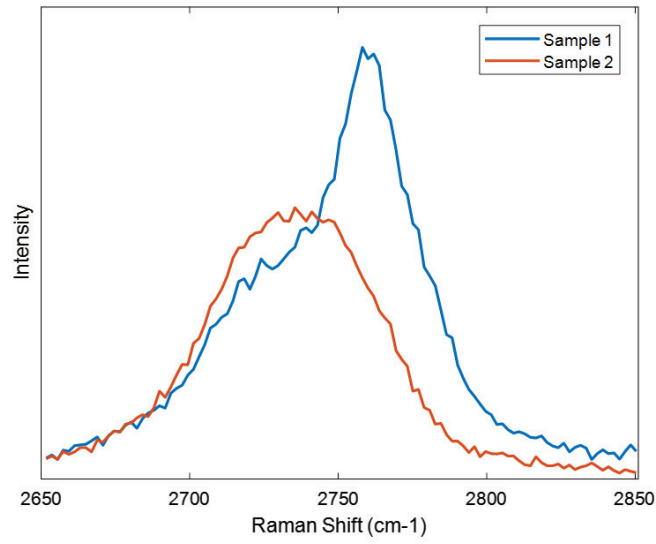


FIG. 4. Characterized layer number of graphene flakes by Raman spectroscopy. Sample 2 (7-layers) corresponds to the sample presented in the main text and sample 1, a three layer graphene as reference.

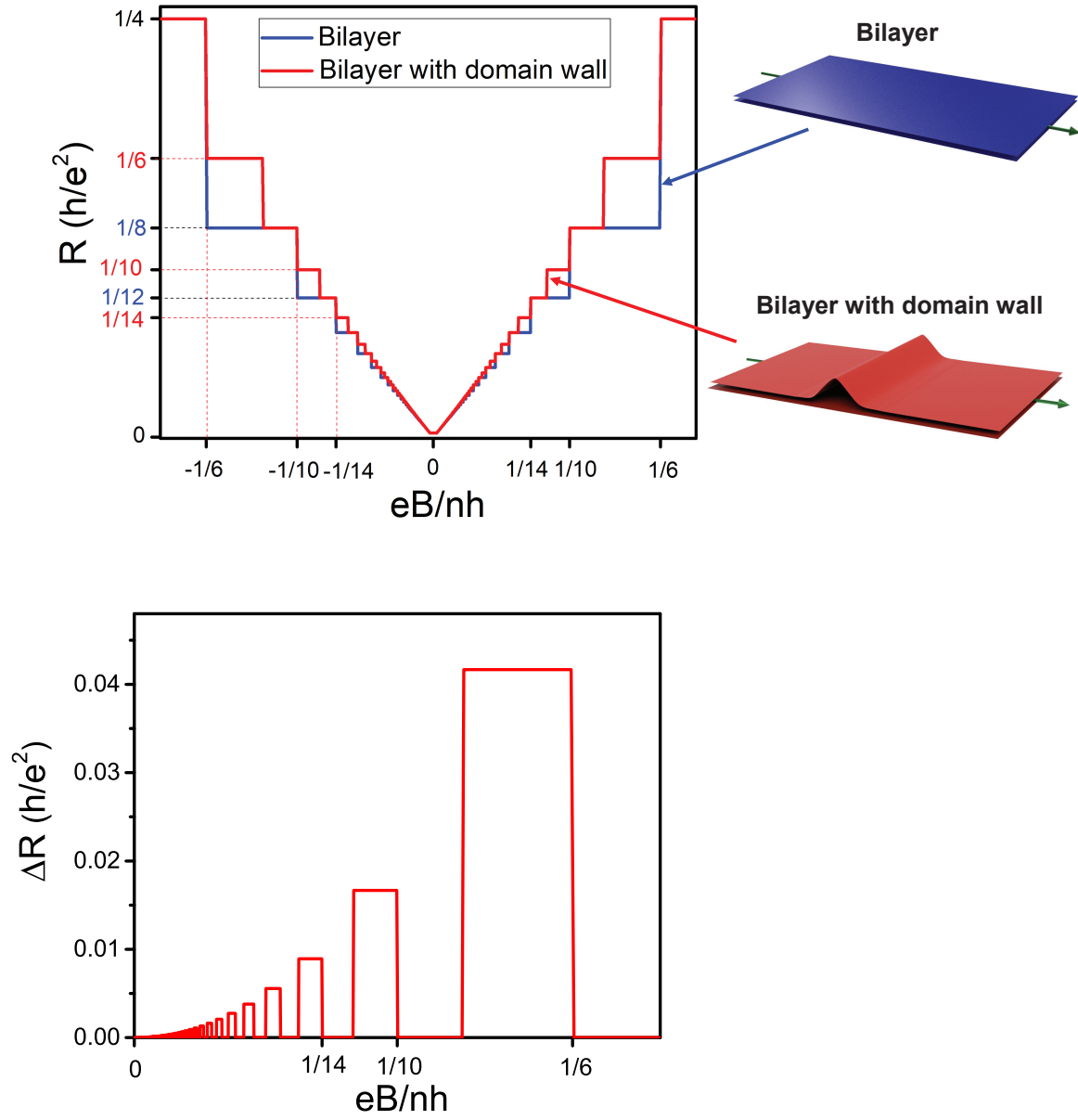


FIG. 5. **Quantum Hall resistance in bilayer graphene** is contrasted with the effect of adding a domain wall orthogonal to the electron transport (top). Bilayer QHE plateaus are indicated in blue. Additional plateaus appear at  $(1/6)(h/e^2)$ ,  $(1/10)(h/e^2)$ ,  $(1/14)(h/e^2)$ ,  $\dots$ , marked in red. Bottom: Magnetoresistance with no domain wall subtracted from the magnetoresistance with a domain walls, or difference between the red and blue curves at the top.

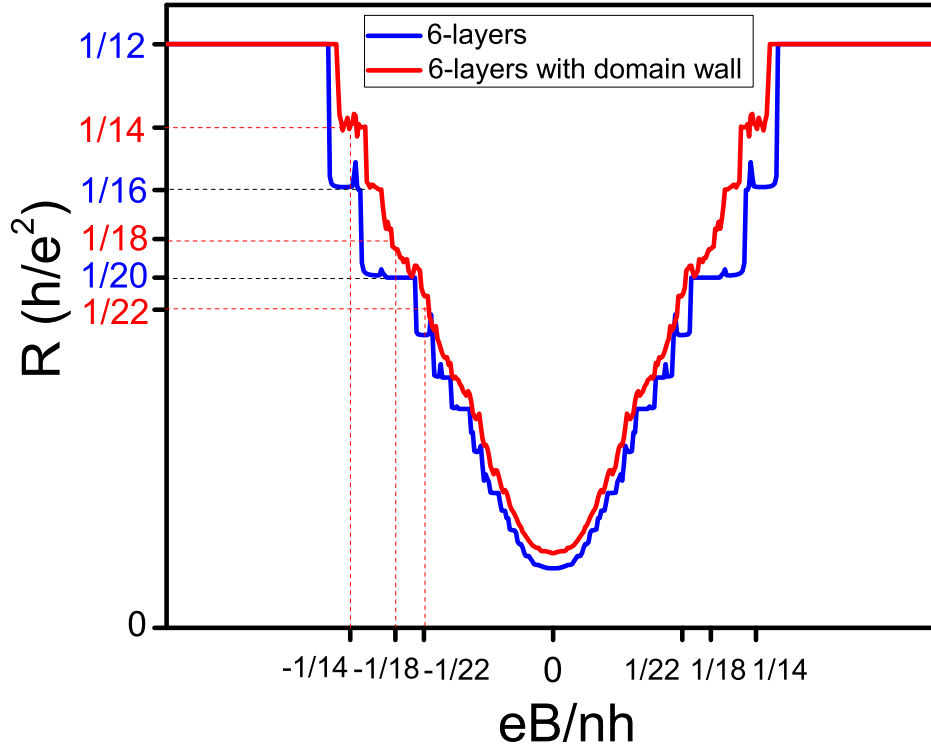


FIG. 6. **Quantum Hall resistance in six-layer graphene** is contrasted with the effect of adding a domain wall orthogonal to the electron transport (top). Six-layer QHE plateaus are indicated in blue. Additional are expected at  $(1/14)(h/e^2)$ ,  $(1/18)(h/e^2)$ ,  $(1/22)(h/e^2)$ ,  $\dots$ , marked in red.

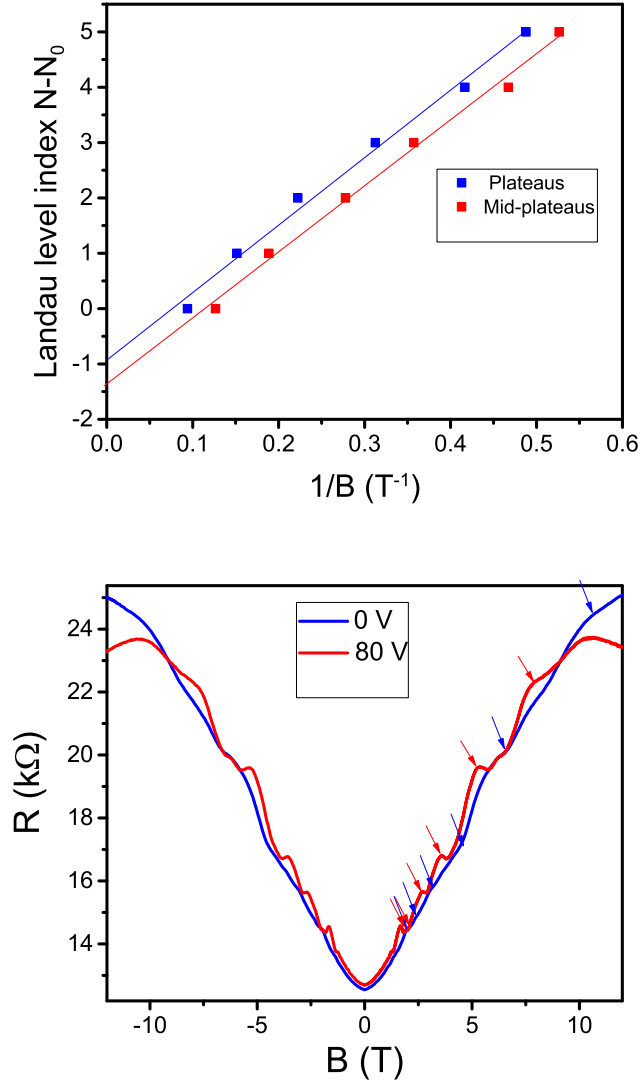


FIG. 7. **The fan diagram of the observed QHE features** is represented. Top: Index of the lowest Landau level observed  $N_0$  subtracted from the sequence of observed Landau levels  $N$  as a function of the inverse of the magnetic field  $1/B$ . Blue dots correspond to the QHE features observed in the data in the absence of strain. Red dots correspond to the QHE features observed in the data when strain is imposed on the sample by applying 80 V on the actuators. Linear fits to the data show a intercept with the y-axis at -1 in the case of the data with no strain and -1/2 for the data in the presence of strain, in consistency with equations 2, 3, 5 and 4. Bottom: arrows indicate the QHE features represented in the fan diagram, extracted from the magnetoresistance data in the absence of strain (0V) and with 80 V applied to the actuators.

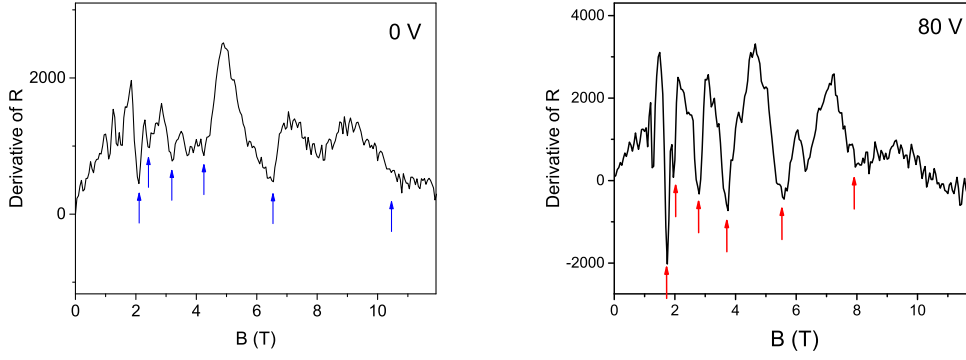


FIG. 8. **Methodology to identify QHE features in the magnetoresistance.** Derivative of the magnetoresistance for 0 V (left figure) and 80 V (right figure) applied on the actuators. Arrows indicate magnetic field values at which QHE features are identified as plateaus (blue, left figure) and mid-plateaus (red, right figure) and represented as a fan diagram in Fig. 7.

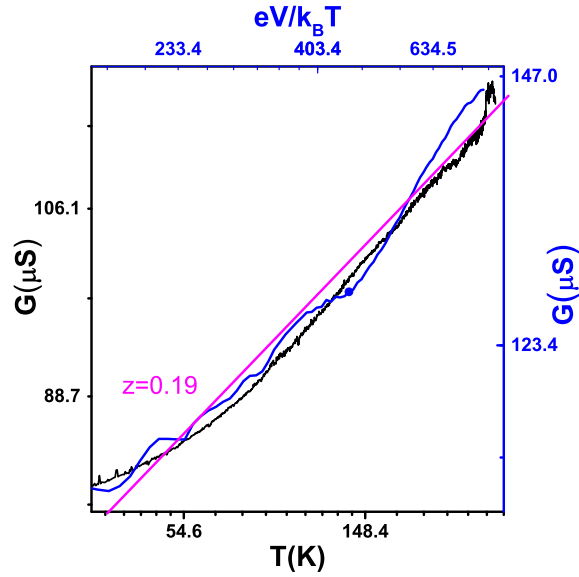


FIG. 9. Temperature dependence of the conductance (left-Bottom axis) compared to the bias-dependent differential conductance (right-top axis) in a double logarithmic scale. Purple line shows a fit to equation 6 with exponent  $z = 0.19$

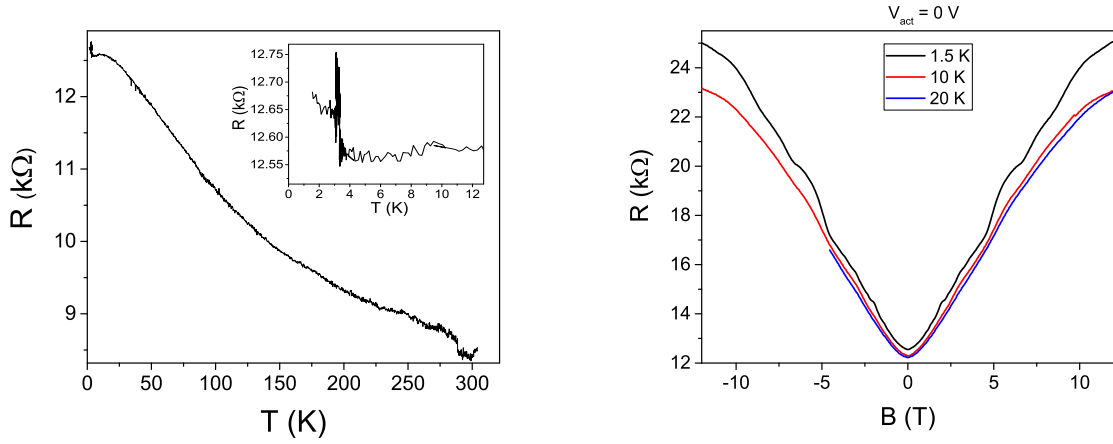


FIG. 10. Left: Temperature dependence of the resistance of the 6-7 graphene sample in the absence of strain in a temperature range 1.5 K-304 K. The inset shows a detail of the temperature range 1.5K-12K. Right: Magnetoresistance with no voltage applied to the actuators at 1.5 K, 10 K and 20 K.

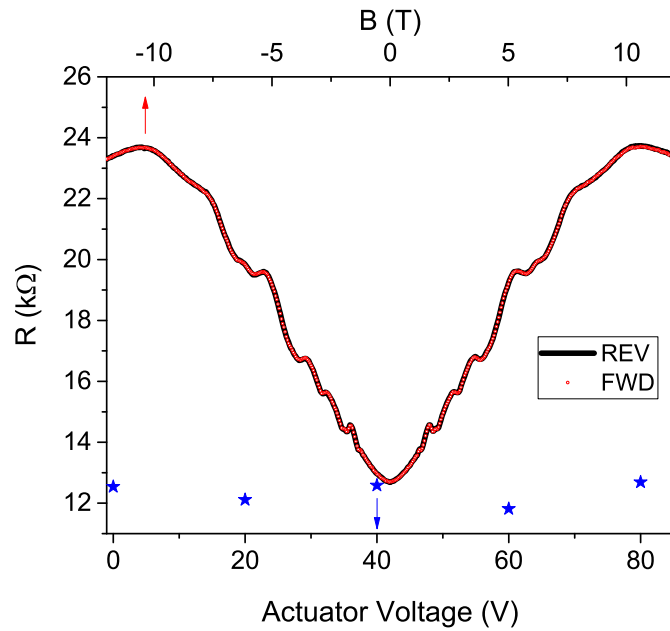


FIG. 11. Magnetoresistance taken with 80V applied to the actuator at 1.5K (top axis) contrasted with the effect of the actuator voltage on the resistance of the sample at 0T (bottom axis). The star symbols correspond to the value of the resistance at zero magnetic field extracted from magnetoresistance measurements run at different voltages on the actuators.

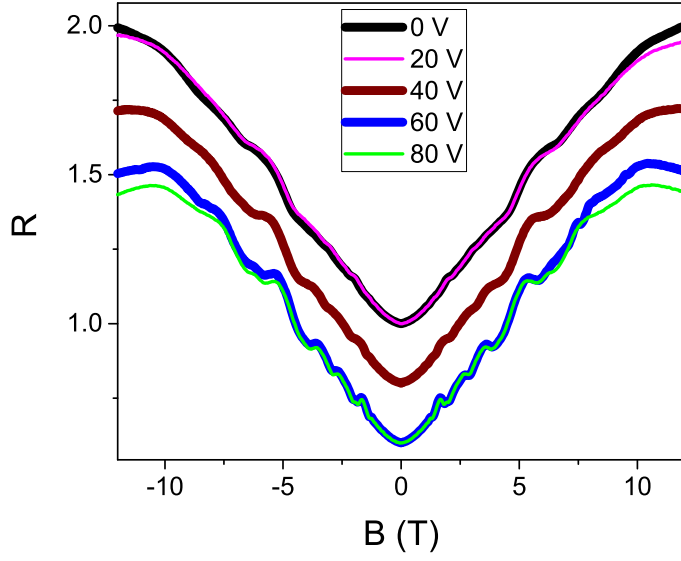


FIG. 12. Magnetic field dependence of the resistance for different voltages on the actuator. Each curve has been normalized by the value of the resistance at zero field, to remove the effect of the different contact resistances at each measurement as detailed in the previous section. Curves for 0 V and 20 V are represented on top of each other (as well as curves for 60 V and 80 V) in order to illustrate similar features of the magnetoresistance. Curves have been shifted for clarity.

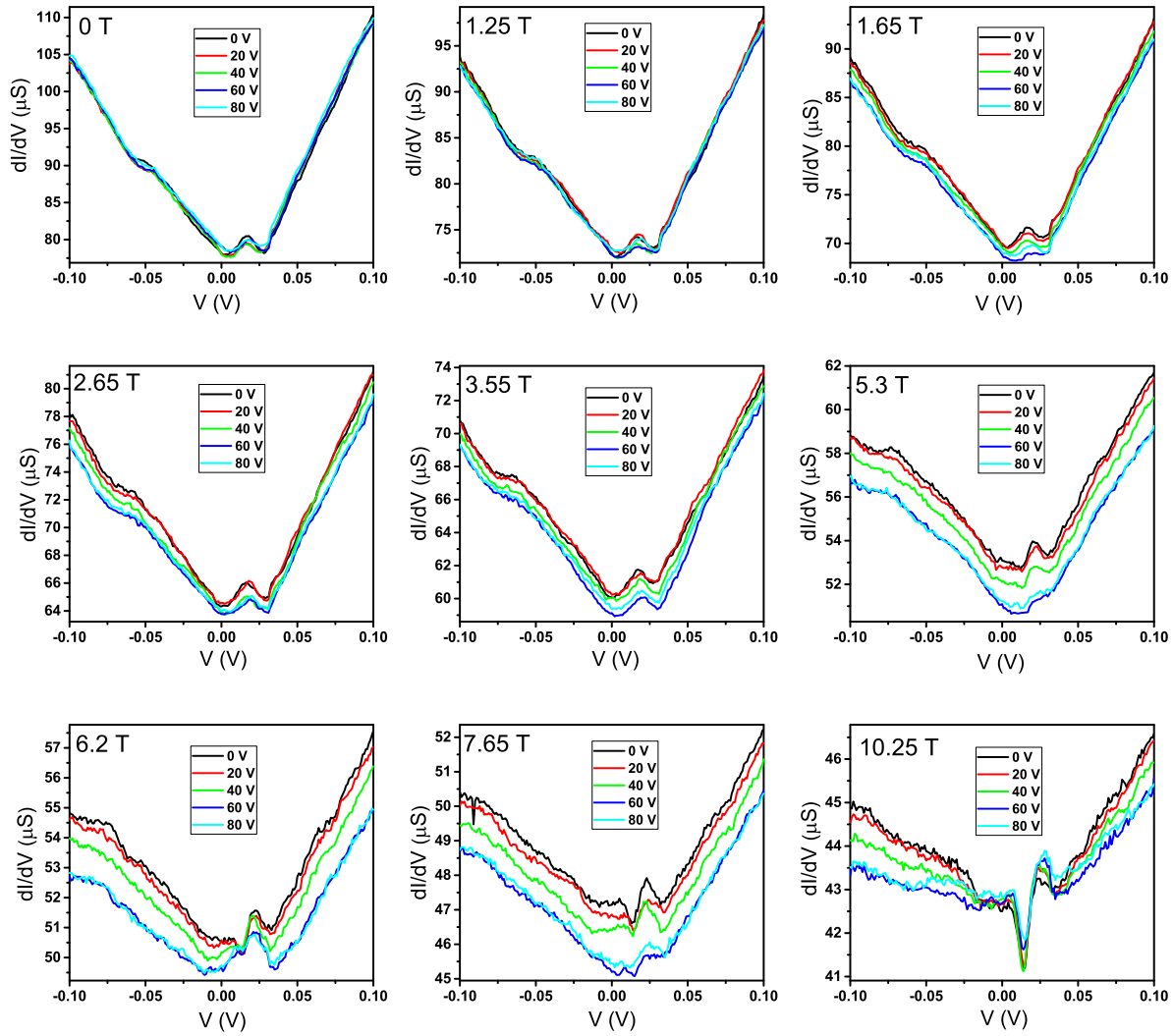


FIG. 13. Differential conductance as a function of the bias voltage for different voltages on the actuator. Each panel shows data taken at a certain magnetic field (0T, 1.25T, 1.65T, 2.65T, 3.55T, 5.3T, 6.2T, 7.65T, 10.25T)